J. Plasma Phys. (2021), *vol*. 87, 905870212
Published by Cambridge University Press
doi:10.1017/S0022377821000258

Effect of driving frequency on dust particle dynamics in radiofrequency capacitive argon discharge

Abdelhak Missaoui [1],†, **Morad El kaouini**[2] **and Hassan Chatei**[1]

[1]Laboratory of Physics of Matter and Radiation, Faculty of Sciences, Mohammed I University, Oujda 60040, Morocco

[2]LMASI, Electromagnetism, Physics of Plasmas and Applications, Polydisciplinary Faculty of Nador, Selouane 62700, Morocco

(Received 20 October 2020; revised 23 February 2021; accepted 25 February 2021)

This paper investigates the influence of the driving frequency on the dynamics of a single dust particle in argon radiofrequency discharge. A one-dimensional fluid model is presented and solved in the entire inter-electrode domain using the finite difference method. In order to solve the particle equation of motion, the coefficients describing the amplification and the damping of the dust particle oscillations are analytically calculated around the equilibrium position, these coefficients allow us to find the relation between the plasma and dust parameters. The results obtained cover the discharge characteristics, the charge and the dynamics of the dust particle. It has been found that the driving frequency has a significant effect on not only the discharge properties but also on the damped oscillatory motion and the equilibrium position of the dust particle. Hence, these oscillations become closer to the electrodes with increasing driving frequency whereas the dust equilibrium position becomes relatively farther from the powered electrode when the dust size decreases.

Key words: electric discharges, dusty plasmas, complex plasmas

1. Introduction

Capacitively coupled radiofrequency (RF) plasma discharges have been widely used in industry. It remains a standard tool for plasma processing applications used in microelectronics and solar cell manufacturing, including etching and thin film depositions (Surendra & Graves 1991; Graves 1994; Bogaerts, Neyts & Gijbels 2002). In order to optimize these applications, it is important to understand the physical characteristics and the effect of the operating parameters on the discharge behaviour.

Many operating parameters can influence the discharge characteristics such as the gas pressure, the applied voltage, the gap between electrodes and the driving frequency, which is an important operating parameter in capacitive glow discharges. Thus, many researchers have studied the effect of the driving frequency on the discharge characteristics (Surendra & Graves 1991; Vahedi *et al.* 1993; Colgan, Meyyappan & Murnick 1994; Heintz &

† Email address for correspondence: abdelhakmissaoui92@gmail.com

Hieftje 1995; Kitajima *et al.* 1998; Rakhimova *et al.* 2006; Zhu *et al.* 2007; Liu *et al.* 2012; Huang & Gudmundsson 2014; Wilczek *et al.* 2015; Sharma *et al.* 2016; Samir *et al.* 2017; Liu, Booth & Chabert 2018; Sharma *et al.* 2018). These studies have shown a significant change in the discharge properties with a change in the driving frequency. Colgan *et al.* (1994) studied the electrical characteristics of argon discharges at different frequencies varying from 13.56 to 54.4 MHz. They observed that electron density varies with the square of driving frequency at a given pressure and applied voltage. By particle-in-cell/Monte Carlo collision simulations and analytical modelling, Wilczek *et al.* (2015) investigated the effect of driving frequency varied from 50 to 90 MHz on the plasma density and the electron dynamics in a capacitive RF argon plasma operated at low pressure. They found an increase in the ion density at the electrodes by a factor of approximately 4 and an increase in the electron density on space and time average by a factor of approximately 13 when the driving frequency increases from 59 to 60 MHz. Furthermore, Samir *et al.* (2017) investigated the effect of driving frequency on the electron heating mechanism in capacitively coupled argon discharge, by using a fluid approach. They found a decrease in the sheath width as the driving frequency increases from 3.39 to 27.12 MHz. Meanwhile, the electron heating increases in the sheaths owing to the high electric field in this regions. These studies assumed that no dust particles are in the discharge despite the presence of these particles in RF capacitive discharges being a common phenomenon. The dust particles in RF reactors can be generated in processing plasma owing to etching and sputtering of wall material (Mikikian *et al.* 2010), or formed in chemically active plasmas in three phases: nucleation, microscopic particle growth by coagulation and further growth by the attachment of the radicals on particle surfaces (Bleecker, Bogaerts & Goedheer 2006). In addition, the dust particles can be immersed from the outside into the discharge (Schabel *et al.* 1999).

The modelling of dust particles in RF capacitive glow discharges has been the subject of much research to understand the physics of this problem. However, some previous studies on dust particles in RF reactors have only considered plasma sheaths (Nitter 1996; Ivlev, Konopka & Morfill 2000; Tomme, Annaratone & Allen 2000; El kaouini, Chatei & Bougdira 2014). The fluid model studies that take into account the whole plasma domain, including both the plasma bulk and the sheaths, are uncommon. Meanwhile, these studies mostly consider the well-known local field approximation (LFA) instead of the electron energy balance by assuming a local equilibrium between charged particle kinetics and electric field (Boeuf 1987; Davoudabadi & Mashayek 2006; Horn, Davoudabadi & Shotorban 2011). However, this assumption has always been limited to describe the plasma discharges, which require a sufficiently good characterization of the charged particles determining the plasma characteristics. Boeuf (1987) found that the local equilibrium assumption can provide realistic results but in a limited range of applied voltage, whereas Grubert, Becker & Loffhagen (2009) strongly recommended the local mean energy approximation (LMEA) where an electron energy equation can be added, removing the local field assumption, they found that the application of the LFA is inappropriate for the analysis of RF plasma discharges, because it can break down when field-reversal situations occur during the temporal evolution of the plasma.

In this work, a time-dependent fluid model of capacitive discharge including the energy balance equation of electrons is established and numerically solved using the finite difference method. Moreover, we have analytically calculated the coefficients describing the amplification and the damping of oscillation of an injected dust particle owing to the influence of the electric force, the ion drag force and neutral drag force, to find the relation between the plasma characteristics and the dust particle parameters. In addition, we focus on the effect of the driving frequency on the dust particle dynamics

https://doi.org/10.1017/S0022377821000258 Published online by Cambridge University Press

and damped oscillations. In the rest of this work, we discuss the fluid model and the discharge characteristics in § 2. In § 3, the charging model is presented and discussed for a micrometre-sized dust particle at three different frequencies. In §§ 4 and 5 the forces acting on the dust particle and the result of the dust dynamic are given, respectively. Finally, conclusions are drawn in § 6.

2. RF argon plasma discharge

A one-dimensional (1-D) RF discharge between two symmetric parallel-plate electrodes separated by a distance of $D = 2.54$ cm is simulated. The RF discharge is filled with the argon gas at a pressure of 1 Torr and sustained by a sinusoidal external excitation $V = V_{\rm rf}\sin(2\pi ft)$ at $x = 0$ applied to the lower electrode where f is the driving frequency, whereas the electrode at $x = D$ (upper electrode) is grounded. In order to describe the behaviour of an isolated dust particle in the discharge, we adopt for the plasma species a self-consistent fluid approach in drift-diffusion approximation. In addition, in order to examine the dynamics of dust we inject a spherical dust particle into the discharge as shown in figure 1. Assuming that the dust particle has no effects on the discharge characteristics, hence, the system of equations describing the discharge will be solved independently.

2.1. *RF fluid model*

The RF discharge model used in this study is based on the fluid description of the electrons and ions including the continuity equation, momentum balance equation and electron energy balance equation coupled with Poisson's equation. The continuity equations for electrons and positive ions are derived from Boltzmann equation and the particles fluxes are described by the drift-diffusion approximation (Zhao, Liu & Samir 2018)

$$\frac{\partial n_{e,i}}{\partial t} + \frac{\partial \Gamma_{e,i}}{\partial x} - R_i = 0, \tag{2.1}$$

$$\Gamma_{e,i} = \mp n_{e,i}\mu_{e,i}E - D_{e,i}\frac{\partial n_{e,i}}{\partial x}, \tag{2.2}$$

where $n_{e,i}$ is the number density of electrons and ions, R_i is the source term that contains only the rate of ionization reaction and $\Gamma_{e,i}$ represent the fluxes of electrons and ions. In (2.2), $\mu_{e,i}$ and $D_{e,i}$ are the mobilities and the diffusion coefficients of the electrons and the ions. The energy balance of electrons has been also derived from the Boltzmann equation and it is introduced to investigate the electron temperature T_e along the inter-electrode discharge. It can read as follows

$$\frac{\partial}{\partial t}\left(\frac{3}{2}n_e k_B T_e\right) + \frac{\partial q_e}{\partial x} + e\Gamma_e E + H_i R_i = 0, \tag{2.3}$$

where T_e is the electron temperature, and E, H_i and k_B are the electric field, the energy loss coefficient with ionization and the Boltzmann constant, respectively. The heat flux of electron energy q_e and electron heating rate $P_{\rm heat}$ coming from the electron current are expressed as

$$q_e = -\kappa_e\frac{\partial T_e}{\partial x} + \frac{5}{2}k_B T_e\Gamma_e, \tag{2.4}$$

$$P_{\rm heat} = e\Gamma_e E = eD_e\frac{\partial n_e}{\partial x}E + e\mu_e n_e E^2, \tag{2.5}$$

https://doi.org/10.1017/S0022377821000258 Published online by Cambridge University Press

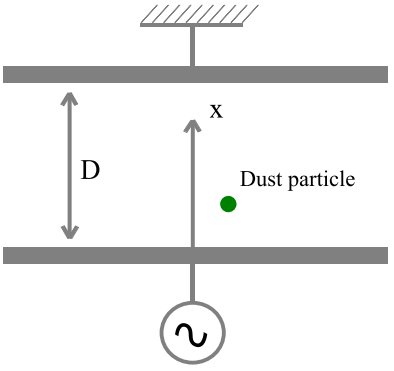

FIGURE 1. Schematic of argon RF capacitive discharge with an injected dust particle.

respectively, where $\kappa_e = 3(k_B D_e n_e)/2$ is the electron thermal conductivity coefficient. Finally, the Poisson equation is used to calculate self-consistently the electric field created by the charged particles in the discharge domain. This equation connects the gradient of the electric field to the densities of charged particles as follows

$$\frac{\partial^2 V}{\partial x^2} = \frac{e}{\varepsilon_0}(n_e - n_i), \tag{2.6}$$

$$E = -\frac{\partial V}{\partial x}. \tag{2.7}$$

In (2.6), ε_0 and e are the permittivity of free space and the elementary charge, respectively.

2.1.1. *Boundary conditions*

The mathematical problem requires the resolution of the coupled system of (2.1)–(2.3) and (2.6) with a set of adequate boundary conditions. Here we have adopted the same boundary conditions that those used in previous papers (Lymberopoulos & Economou 1993; Samir *et al.* 2017).

At the bottom electrode ($x = 0$)

$$\Gamma_i = n_i \mu_i E, \quad \Gamma_e = -k_s n_e - \gamma \Gamma_i, \quad T_e = 0.5 \text{ (eV)} \quad \text{and} \quad V = V_{\text{rf}} \sin(2\pi f t). \tag{2.8a–d}$$

At the top electrode ($x = D$)

$$\Gamma_i = n_i \mu_i E, \quad \Gamma_e = k_s n_e - \gamma \Gamma_i, \quad T_e = 0.5 \text{ (eV)} \quad \text{and} \quad V = 0 \text{ (V)}. \tag{2.9a–d}$$

where γ is the secondary electron emission coefficient and k_s is the electron recombination coefficient.

2.1.2. *Initial conditions*

The initial conditions used in this work are similar to those given by Samir *et al.* (2017) and Zhao *et al.* (2018)

$$n_e = n_i = n_\varepsilon \left[\varepsilon + 16\left(1 - \frac{x}{D}\right)^2 \left(\frac{x}{D}\right)^2\right], \quad T_e = 1 \text{ (eV)} \quad \text{and} \quad V = 0 \text{ (V)}, \tag{2.10a–c}$$

where ε is a small positive number and n_ε is the value of the initial charged particles densities. The remainder of the parameters used in this simulation can be found in table 1.

https://doi.org/10.1017/S0022377821000258 Published online by Cambridge University Press

Coefficient (unit)	Symbol	Value
Neutral density (cm^{-3})	n_n	3.22×10^{16}
Electron diffusivity ($cm^{-1}\,s^{-1}$)	$n_n D_e$	3.86×10^{22}
Electron mobility ($V^{-1}\,cm^{-1}\,s^{-1}$)	$n_n \mu_e$	9.6×10^{21}
Ion diffusivity ($cm^{-1}\,s^{-1}$)	$n_n D_i$	2.07×10^{18}
Electron recombination coefficient ($cm\,s^{-1}$)	k_s	1.19×10^{7}
Electron energy loss (eV)	H_i	15.7
Inter-electrodes distance (cm)	D	2.54
Secondary electron emission	γ	0.01

TABLE 1. Data used in calculation (Lymberopoulos & Economou 1993).

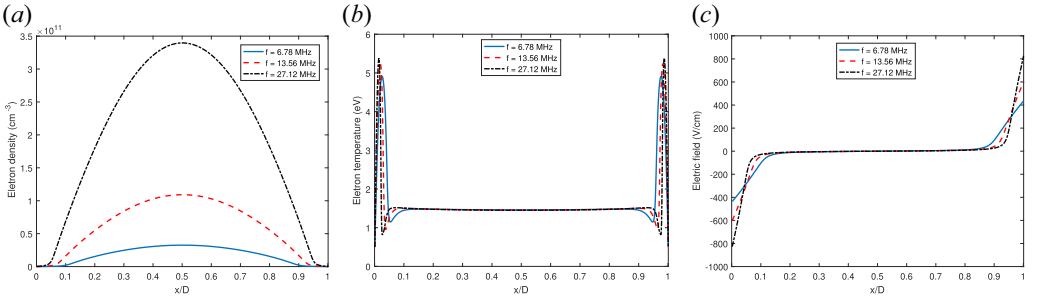

FIGURE 2. The cycle-averaged distributions at different frequencies of (*a*) the electron density, (*b*) the electron temperature and (*c*) the electric field. Conditions are 1 Torr pressure and secondary electron emission coefficient $\gamma = 0.01$. The profiles show the discharge characteristics during the 5000th RF cycle.

2.2. *Discharge characteristics*

Figure 2 shows the cycle-averaged profiles of the electron density, electron temperature and electric field at different driving frequencies 6.78, 13.56 and 27.12 MHz. As one can see in figure 2(*a*), the cycle-averaged electron density is higher in the middle of the plasma discharge (bulk region). However, it is lower in the sheath regions close to the electrodes. The results also show that the electron density increases as the driving frequency increases. In the bulk plasma region, the electron density n_e increases rapidly with the driving frequency and can reach 3.39×10^{11} cm^{-3} at 27.12 MHz. However, this increase is less important near the electrodes. This is because with the growth of the driving frequency, more electrons are accelerated toward the opposite electrode during the sheath expansion, leading to high ionization close to the sheath edge.

The electron temperature is given in figure 2(*b*). It is shown that the profiles are peaked in the sheath regions near the electrodes. These peaks become stronger and narrower when the driving frequency increases from 6.78 to 27.12 MHz. Hence, the sheath width decreases. This fact is due to the high electric field which also increases in the sheaths with the growth of driving frequency as shown in figure 2(*c*). Thus, more electrons will gain energy from the electric field in the sheaths to reach the ionization threshold energy which leads to a high electron production rate (Zhao *et al.* 2016). The maximum electron temperature rises in the sheath regions and changes from 4.91 eV at 6.78 MHz to 5.38 eV at 27.12 MHz. However, T_e remains constant around 1.45 eV in the bulk plasma region.

https://doi.org/10.1017/S0022377821000258 Published online by Cambridge University Press

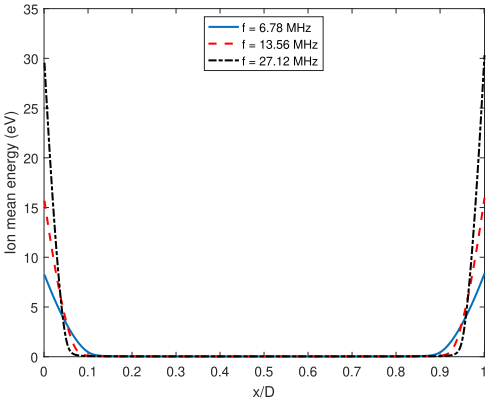

FIGURE 3. The spatial distributions of the ion mean energy E_i for three different frequencies 6.78, 13.56 and 27.12 MHz in Ar capacitive discharge at 1 Torr.

These results agree well with the earlier studies by Samir *et al.* (2017) with small difference in the electron temperature in the pre-sheath region, where a decrease in electron temperature is observed because of the cooling mechanism of electrons in this region. Figure 3 shows the ion mean energy as a function of the normalized distance between electrodes at different frequencies. In the sheath regions, it is shown that the ion mean energy is higher and increases with the driving frequency owing to the strong electric field in this regions (see figure 2*c*). In the bulk region, the ion mean energy is low and approximately 0.032 eV owing to the weak electric field in this region. Hence, the ion mean energy is mainly determined by the electric field. It should be noted that despite the differences in the operating conditions, the discharge characteristics obtained by the fluid model code show that the calculated data are in satisfactory agreement with the particle-in-cell calculations given by Benyoucef *et al.* (2010).

3. Charging of the dust particle

A dust particle in a RF plasma acts as a small floating object and collects ions and electrons. However, for a spherical dust particle with radius r_d, the electron and positive ion currents at the dust surface can be calculated using orbital-motion-limited (OML) theory when the condition $r_d \ll \lambda_L$ applies, where $\lambda_L = [(1/\lambda_{De})^2 + (1/\lambda_{Di})^2]^{-1/2}$ is the linearized Debye length. These orbit-limited currents are given by (Akdim & Goedheer 2003)

$$I_e = 4\pi r_d^2 e n_e \sqrt{\frac{k_B T_e}{2\pi m_e}} \exp\left(\frac{eV_{fl}}{k_B T_e}\right), \tag{3.1}$$

$$I_i = 4\pi r_d^2 e n_i \sqrt{\frac{k_B T_i}{2\pi m_i}} \left(1 - \frac{eV_{fl}}{k_B T_i}\right), \tag{3.2}$$

where m_i and m_e are the ion and electron masses, T_e and T_i are the ion and electron temperatures and V_{fl} is the floating potential at the surface of the dust.

Recent works by Matthews *et al.* (2020), Khrapak *et al.* (2005) and Land *et al.* (2010) have shown the importance of ion–neutral collisions for the charging of dust in plasma. In order to take into account the collision of ions with the neutral particles, a modified formula for ion current is used to replace (3.2) and is given by Land *et al.* (2010) based on

https://doi.org/10.1017/S0022377821000258 Published online by Cambridge University Press

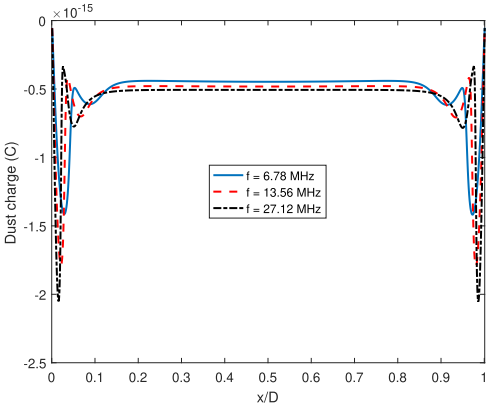

FIGURE 4. The spatial distributions of the dust charge for three different frequencies 6.78, 13.56 and 27.12 MHz corresponding to $r_d = 1.5$ μm in Ar capacitive discharge at 1 Torr.

the previous study by Khrapak *et al.* (2005):

$$I_i = 4\pi r_d^2 e n_i \sqrt{\frac{E_i}{2m_i}} \left[1 - \frac{eV_{fl}}{E_i} + 0.1 \left(\frac{eV_{fl}}{E_i} \right)^2 \frac{\lambda_L}{l_{mfp}} \right]. \tag{3.3}$$

The mean energy E_i for ions is adopted to take into account the drift component of the ion velocity (Akdim & Goedheer 2003; Bleecker *et al.* 2006; Goedheer & Land 2008)

$$E_i = \frac{1}{2} m_i v_s^2 = \frac{4k_B T_g}{\pi} + \frac{1}{2} m_i v_i^2, \tag{3.4}$$

where the first part is the ion thermal energy and the second part is a kinetic energy from the drift velocity.

The ions current in (3.3) depends on the mean free path and the linearized Debye length around the dust particle because ions near the dust can lose their angular momentum when they collide with neutral particles. If the ions are close enough to the dust, they can be collected, which increases the ion current and reducing the negative floating potential. Making (3.1) and (3.3) equal, the floating potential V_{fl} of the dust particle is obtained. Then, the dust charge is determined by using

$$Q_d = 4\pi\epsilon_0 r_d V_{fl}. \tag{3.5}$$

Figure 4 represents the distribution of the dust charge as a function of the distance between electrodes at different driving frequencies and with particle radius 1.5 μm. As we can see, the charge accumulated on the particle is larger and negative near the electrodes because of the high electron temperature in these two sheath regions. However, in the bulk plasma region, the charge is lower because of the weak electric field and low electron temperature. Moreover, the maximums of the dust charge change and move toward the electrodes when the driving frequency increases from 6.78 to 27.12 MHz in the sheath regions, because of the growth in the electric field with the driving frequency. However, the charge slightly increases in the bulk region.

4. Forces acting on the dust particle

In the present model, we consider the gravitational, electric, neutral drag and ion drag forces, which are expected to be important, whereas the thermophoretic force is neglected.

https://doi.org/10.1017/S0022377821000258 Published online by Cambridge University Press

The gravitational force is given by

$$F_g = \tfrac{4}{3}\pi r_d^3 \rho_d g, \tag{4.1}$$

where g is the gravitational acceleration, r_d is the dust particle radius and ρ_d is the mass density of the dust particle. The electric force is given by

$$F_e = Q_d E, \tag{4.2}$$

where E is the electric field and Q_d is the dust particle electric charge.

The neutral drag force due to the collision of dust particle with neutral gas is taken to be of the following form (Epstein 1924; Nitter 1996)

$$F_n = -\frac{16}{3}\sqrt{\pi} r_d^2 n_n k T_g s \left(1 + \frac{\pi}{8}\right), \tag{4.3}$$

where n_n is the density of the neutral gas atoms. Here $s = v_d/v_{th,n}$, with v_d is the dust velocity and $v_{th,n}$ is the neutral thermal velocity. In our discharge plasma conditions with argon, $P = 1$ Torr, $m_n = 6.64 \times 10^{-26}$ kg and $T_g = 300$ K, the dust particle velocity is always much lower than the neutral thermal velocity ($v_d \ll v_{th,n}$). Thus, in this case the Epstein's expression for the neutral drag force is appropriate (Nitter 1996).

The total ion drag force resulting from the momentum transfer from the ions following the dust particle is the sum of the collection force F_i^{coll} due to the direct hitting by ions and the Coulomb force F_i^{coul} due to Coulomb scattering of ions by the charged dust. Different approaches have been used to calculate the ion drag force (Khrapak *et al.* 2002; Ivlev *et al.* 2004; Hutchinson 2006; Goedheer, Land & Venema 2009; Khrapak 2013). In our case, we adopt the same expression as Goedheer *et al.* (2009) who considered the collisions between ions and neutrals by incorporating the results of previous studies (Khrapak *et al.* 2002; Ivlev *et al.* 2004; Hutchinson 2006). The total ion drag force is given by

$$\begin{aligned} F_i &= F_i^{\text{coll}} + F_i^{\text{coul}} \\ &= n_i m_i v_s v_i \times \left(\sigma_c(v_s) + \pi \rho_0^2(v_s)\left[\Gamma(v_s) + \mathcal{K}\left(\frac{\lambda_L(v_s)}{l_{mfp}}\right)\right]\right), \end{aligned} \tag{4.4}$$

where

$$\mathcal{K}(x) = x \arctan(x) + \left(\sqrt{\frac{\pi}{2}} - 1\right)\frac{x^2}{1+x^2} - \sqrt{\frac{\pi}{2}}\ln\left(1 + x^2\right) \tag{4.5}$$

is a collisional function to take into account loss of angular momentum in collisions of ions and background neutrals (Ivlev *et al.* 2005), σ_c is the ion capture cross section given by

$$\sigma_c\,(v_s) = \pi r_d^2 \left(1 + \frac{\rho_0\,(v_s)}{r_d}\right) \tag{4.6}$$

and $\rho_0 = Ze^2/2\pi\epsilon_0 m_i v_s^2$ is the Coulomb radius where Z is the number of electron charges on the dust particle. To include ions scattered beyond the screening length, the expression of the Coulomb logarithm is given by (Khrapak *et al.* 2002)

$$\Gamma = \ln\left[\frac{\rho_0(v_s) + \lambda_L(v_s)}{\rho_0(v_s) + r_d}\right]. \tag{4.7}$$

However, this equation is not correct for larger ion drift velocity, hence, an effective ion velocity suggested by Hutchinson (2005) can give a good agreement in the calculation

https://doi.org/10.1017/S0022377821000258 Published online by Cambridge University Press

of the Coulomb logarithm. In our case, we adopt the ion mean velocity using the same approach as Goedheer *et al.* (2009) and Land *et al.* (2010), based on the fitting results from previous studies by Hutchinson (2005)

$$v_s^2 = \frac{8k_B T_g}{\pi m_i} + v_i^2 \times \left[1 + \left(\frac{v_i}{u_b} / \left(0.5 + 0.05 \ln\left(\tilde{m}_i/Z\right) + \left(T_i/T_e\right)^{1/2}\right)\right)^3\right], \tag{4.8}$$

where $\tilde{m}_i$ is the ion mass in amu ($\tilde{m}_i/Z = 40$ for argon ions) and $u_b = (kT_e/m_i)^{1/2}$ is the Bohm velocity (Hutchinson 2005).

Having specified the forces, the equation of motion for the dust particle in the whole discharge can be written in the form

$$m_d \ddot{x} = F_t(x, \dot{x}) = F_2(x) + F_i(x, \dot{x}) + F_n(\dot{x}), \tag{4.9}$$

where F_t represents the total force acting on the dust particle and $\dot{x}$ is the dust velocity. Here, F_2 combines the force of gravity and the electric force.

By linearizing around the equilibrium position $x = x_0$ and $\dot{x} = 0$, equation (4.9) can be expressed as

$$m_d \ddot{x}_1 = \left(\frac{\partial F_2}{\partial x}\right)_{x_0} x_1 + \left(\frac{\partial F_i}{\partial x}\right)_{x_0, \dot{x}=0} x_1 + \left(\frac{\partial F_i}{\partial \dot{x}}\right)_{x_0, \dot{x}=0} \dot{x}_1 + \left(\frac{\partial F_n}{\partial \dot{x}}\right)_{x_0, \dot{x}=0} \dot{x}_1, \tag{4.10}$$

where $x_1 = x - x_0$. As the force of gravity remains constant, equation (4.10) can be written as an equation of the damped harmonic oscillator

$$m_d \ddot{x}_1 = k_2 x_1 + k_3 \dot{x}_1, \tag{4.11}$$

where $k_2 = k_{2e} + k_{2i}$ and $k_3 = k_{3i} + k_{3n}$ describe the coefficient of oscillation and the coefficient of damping caused by the neutral drag and the ion drag forces, respectively. Here, k_{2e} is the coefficient describing the contribution of the electric force, k_{2i} and k_{3i} combine the contribution of the collection and the Coulomb parts of the ion drag force as

$$k_{2i} = k_{2i,\mathrm{coll}} + k_{2i,\mathrm{coul}}, \quad k_{3i} = k_{3i,\mathrm{coll}} + k_{3i,\mathrm{coul}}. \tag{4.12a,b}$$

where the coefficients k_{2e}, $k_{2i,\mathrm{coll}}$ and $k_{2i,\mathrm{coul}}$ are calculated from (4.2) and (4.4) and given by

$$k_{2e} = -4\pi\varepsilon_0 r_d \left[\frac{\partial V_{fl}}{\partial x}\frac{\partial V}{\partial x} + V_{fl}\left(\frac{\partial^2 V}{\partial x^2}\right)\right], \tag{4.13}$$

$$k_{2i,\mathrm{coll}} = m_i n_i v_i \left[\left(\frac{1}{v_i}\frac{\partial v_i}{\partial x} + \frac{1}{n_i}\frac{\partial n_i}{\partial x}\right) v_s \sigma_c + \sigma_c \frac{\partial v_s}{\partial x} + \frac{2\pi e r_d}{m_i v_s^2} \times \left(v_s \frac{\partial V_{fl}}{\partial x} - 2V_{fl}\frac{\partial v_s}{\partial x}\right)\right] \tag{4.14}$$

$$k_{2i,\mathrm{coul}} = \pi m_i n_i v_i \rho_0^2 \left[\left(\Gamma + \mathcal{K}(\lambda_n)\right)\left(\left(\frac{1}{v_i}\frac{\partial v_i}{\partial x} + \frac{1}{n_i}\frac{\partial n_i}{\partial x}\right) v_s + \frac{\partial v_s}{\partial x} + \frac{2}{V_{fl}}\right) + \frac{v_s}{\rho_0 + r_d}\left(\frac{e r_d}{m_i v_s^3}\left(\frac{r_d - \lambda_L}{\rho_0 + r_d}\right)\left(v_s \frac{\partial V_{fl}}{\partial x} - 2V_{fl}\frac{\partial v_s}{\partial x}\right) + \frac{\partial \lambda_L}{\partial x}\right) + v_s\left(\frac{\partial \lambda_n}{\partial x}\arctan\left(\lambda_n\right) - \frac{\lambda_n}{1 + \lambda_n^2} - 2\left(\sqrt{\frac{\pi}{2}} - 1\right)\frac{\lambda_n^3}{\left(1 + \lambda_n^2\right)^2}\right)\right], \tag{4.15}$$

https://doi.org/10.1017/S0022377821000258 Published online by Cambridge University Press

respectively, where $\lambda_n = \lambda_L(v_s)/l_{mfp}$. Moreover, the coefficients $k_{3i,\mathrm{coll}}$, $k_{3i,\mathrm{coul}}$ and k_{3n} are calculated from (4.3) and (4.4) and given by

$$k_{3i,\mathrm{coll}} = -m_i n_i \left[v_s \sigma_c + v_i^2 \left(5 \left(\frac{v_i}{u_b} / \left(0.5 + 0.05 \ln \left(\tilde{m}_i / Z_i \right) + \left(T_i / T_e \right)^{1/2} \right) \right)^3 + 2 \right) \right.$$
$$\left. \times \left(\frac{\sigma_c}{2 v_s} - \frac{2\pi e r_d V_{fl}}{m_i v_s^3} \right) \right] \tag{4.16}$$

$$k_{3i,\mathrm{coul}} = \pi m_i n_i \rho_0^2 v_i^2 \left[\left(\Gamma + \mathcal{K}(\lambda_n) \right) \right.$$
$$\times \left(\frac{v_s}{v_i^2} - \frac{3}{2 v_s} \left(5 \left(\frac{v_i}{u_b} / \left(0.5 + 0.05 \ln \left(\tilde{m}_i / Z_i \right) + \left(T_i / T_e \right)^{1/2} \right) \right)^3 + 2 \right) \right)$$
$$\left. - \frac{v_s}{v_i} \left(\Gamma'' + \mathcal{K}'' \left(\lambda_n \right) \right) \right], \tag{4.17}$$

respectively, where Γ'' and $\mathcal{K}''(\lambda_n)$ denote the derivatives with respect to dust velocity of the Coulomb logarithm and of the collisional function, respectively,

$$\Gamma'' = \frac{1}{\left(\rho_0 + \lambda_L \right) \left(\rho_0 + r_d \right)} \left[\left(r_d - \lambda_L \right) \right.$$
$$\times \left(\frac{e r_d V_{fl}}{m_i v_s^4} v_i \left(5 \left(\frac{v_i}{u_b} / \left(0.5 + 0.05 \ln \left(\tilde{m}_i / Z_i \right) + \left(T_i / T_e \right)^{1/2} \right) \right)^3 + 2 \right) \right)$$
$$\left. - \frac{\lambda_L^3 v_i}{\lambda_{D_i}^2 v_{th,i}^2 \left(1 + \frac{v_i^2}{v_{th,i}^2} \right)} \right], \tag{4.18}$$

$$\mathcal{K}''(\lambda_n) = - \frac{\lambda_L^3 v_i}{l_{mfp} \lambda_{Di}^2 v_{th,i}^2 \left(1 + \frac{v_i^2}{v_{th,i}^2} \right)}$$
$$\times \left[\arctan \left(\lambda_n \right) - \frac{\lambda_n}{1 + \lambda_n^2} - 2 \left(\sqrt{\frac{\pi}{2}} - 1 \right) \frac{\lambda_n^3}{\left(1 + \lambda_n^2 \right)^2} \right] \tag{4.19}$$

and

$$k_{3n} = - \frac{16}{3} \sqrt{\pi} r_d^2 n_n k_B T_g \left(1 + \frac{\pi}{8} \right) \Big/ v_{\mathrm{th},n}. \tag{4.20}$$

From (4.11), it can be shown that the dust particle acts as a damped harmonic oscillator. Hence, the damping time τ_d, the oscillation frequency ω and the oscillation time τ are

https://doi.org/10.1017/S0022377821000258 Published online by Cambridge University Press

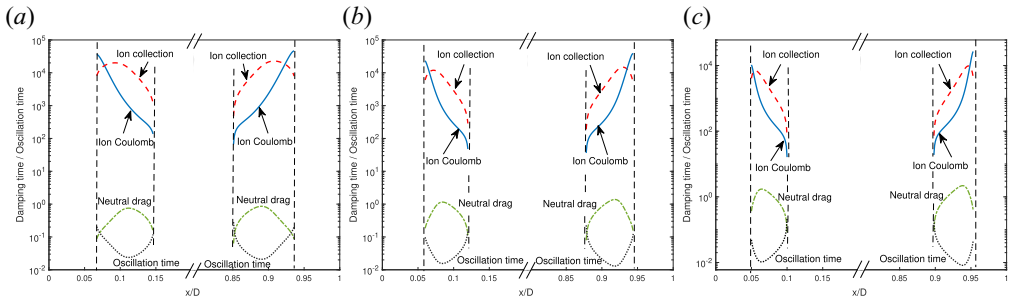

FIGURE 5. The oscillation time in seconds and the damping time compared with the oscillation time due to the ion collection drag (labelled ion collection), ion Coulomb (labelled ion Coulomb) and neutral labelled (neutral drag) for a micrometre-sized $r_d = 1.5$ μm dust particle versus inter-electrode distance at different frequencies (*a*) 6.78 MHz, (*b*) 13.56 MHz and (*c*) 27.12 MHz. Here $\rho_d = 2000\ \mathrm{kg\,m^{-3}}$. The vertical dashed lines indicate the position of the critical points in the discharge.

defined as

$$\tau_d = \frac{2m_d}{|k_3|}, \tag{4.21}$$

$$\omega = \left[-\left(\frac{k_2}{m_d} \right)_{x_0} \right]^{1/2}, \tag{4.22}$$

$$\tau = \frac{2\pi}{\omega}, \tag{4.23}$$

respectively. Calculation of the oscillation and damping parameters described previously yields data on the dust motion in the discharge.

In figure 5, we show the oscillation time in seconds and the damping time compared with the oscillation time (damping time/oscillation time) for the ion collection drag, ion Coulomb drag and neutral drag. The results are obtained for a micrometre-sized dust particle as a function of the normalized inter-electrode distance at three different frequencies 6.78, 13.56 and 27.12 MHz. As we can see, there are some critical points in the discharge domain where the pulsation ω tends to be zero when the dust particle approaches the critical point corresponding to zero oscillation coefficient ($k_2 = 0$), which means that the oscillation time depends on the position in the discharge. In addition, the damping effect due to the neutral drag is more important than that due to ion drag, which indicates that the damping is mainly caused by the neutral drag force. When the driving frequency increases from 6.78 to 27.12 MHz, the oscillation time decreases in the sheath regions from 0.021 to $8.1\times\ 10^{-3}$ s, which means that the oscillation frequency becomes important and the particle oscillates rapidly in these regions.

5. Dust dynamics

Note that we have determined the plasma discharge characteristics in § 2 and the charge and the forces acting on the dust in §§ 3 and 4, we now turn to the dust particle to examine its motion in plasma discharge under the influence of driving frequency by using (4.11).

Figure 6 shows the velocities of a dust particle with $r_d = 1.5$ μm released from the lower electrode given as a function of the position and time for different frequencies. It is seen that this dust particle follows a damped oscillatory motion around its equilibrium

https://doi.org/10.1017/S0022377821000258 Published online by Cambridge University Press

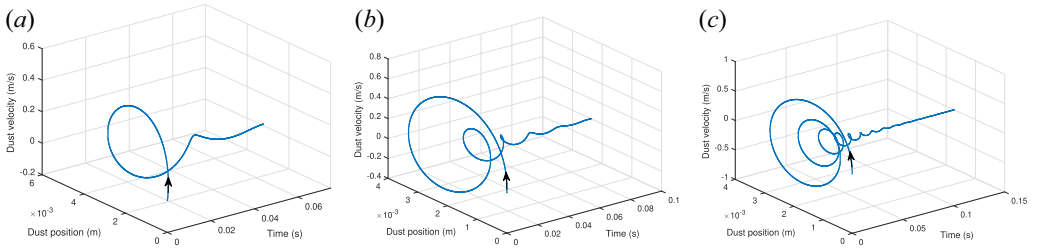

FIGURE 6. The spatiotemporal distributions of a dust particle velocity with $r_d = 1.5$ μm. The dust particle is released from the lower electrode with zero initial velocity $v_d = 0$ m s^{-1} at (*a*) 6.78 MHz, (*b*) 13.56 MHz and (*c*) 27.12 MHz, with $\rho_d = 2000$ kg m^{-3}.

position with higher oscillation frequency when the driving frequency increases, because of the competition between the parameters describing the amplification and the damping of the dust oscillations. In our conditions and for all frequencies, the parameter $k_{3i,\mathrm{coul}}$ is positive around the dust equilibrium position, which means that the contribution of the Coulomb part of the ion drag force is to increase the amplitude of oscillation. However, the parameter $k_{3i,\mathrm{coll}}$ is negative, i.e. the contribution of the collection part of the ion drag force is in the damping of dust oscillation in this position. Meanwhile, k_{3n} is negative, which means that the neutral drag force also acts as a damping force on the dust motion. On the other hand, the location of the dust particle changes and becomes closer to the powered electrode with the growth of the driving frequency because of the reduction in the sheath width and the height from the electrode is reduced from 3.25 to 1.72 mm when the frequency increases from 6.78 to 27.12 MHz. In addition, the oscillation frequency increases because the oscillation time is small near the electrodes compared with that away from electrodes which can be clearly seen in figure 5.

Note that in figure 6, we considered a dust particle with $r_d = 1.5$ μm. To visualize the effect of the dust particle radius on the movement and the equilibrium position in the discharge as a function of the driving frequency, we inject into the discharge an other dust particle with small radius $r_d = 1.1$ μm. Figure 7 gives the velocity as a function of position and time for a dust particle released from the lower electrode without initial velocity, these results are given for three different frequencies 6.78, 13.56 and 27.12 MHz. In all cases, the figures 7(*a*), 7(*b*) and 7(*c*) show that this dust particle also follows a damped oscillatory motion around its equilibrium position with different oscillation frequencies. Moreover, the height from the electrode is reduced from 3.40 to 1.75 mm when the driving frequency increases from 6.78 to 27.12 MHz, which means that this small particle with $r_d = 1.1$ μm levitates relatively away from the electrode with lower oscillation frequency compared with the large dust particle with $r_d = 1.5$ μm (see figure 6). These results agree with the experimental data given by Tomme *et al.* (2000) which show that the particle with a large size levitates closer to the electrode than the particle with a small radius.

Many parameters can influence the possibility of suspension of the injected dust particle, for example, plasma parameters, initial particle position and velocity, particle shape and mass density. Figure 8 illustrates the position as a function of time for a dust particle with $r_d = 1.1$ μm released from two different positions (from the middle and from the upper electrode) without initial velocity. In all cases, when the release is from the upper electrode, the dust particle can be levitated near the sheath edge with higher oscillation frequency when the driving frequency increases. On the other hand, when the release is from the middle of the discharge, the dust particle oscillates near the sheath region of the powered electrode at 6.78 MHz, while its movement ends by hitting the powered

https://doi.org/10.1017/S0022377821000258 Published online by Cambridge University Press

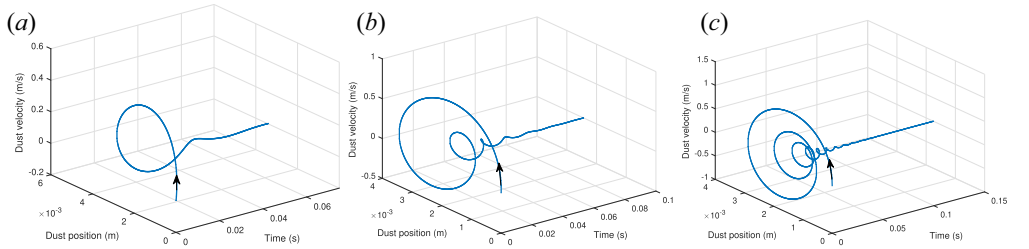

FIGURE 7. The spatiotemporal distributions of a dust particle velocity with $r_d = 1.1$ μm. The dust particle is released from the lower electrode with zero initial velocity $v_d = 0$ m s^{-1} at (*a*) 6.78 MHz, (*b*) 13.56 MHz and (*c*) 27.12 MHz, with $\rho_d = 2000$ kg m^{-3}.

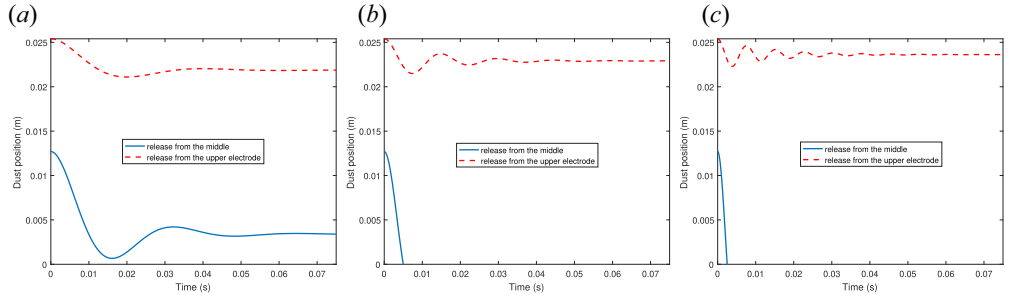

FIGURE 8. The trajectory of the dust particle with $r_d = 1.1$ μm and $v_d = 0$ m s^{-1} released from the middle of the discharge and from the upper electrode at (*a*) 6.78 MHz, (*b*) 13.56 MHz and (*c*) 27.12 MHz, with $\rho_d = 2000$ kg m^{-3}.

electrode at 13.56 and 27.12 MHz, because the dust particle accelerates on its trajectory from the bulk region, and the amplitude of the oscillation initially increases. In figure 9, the trajectories of a micrometre-sized dust particle with $r_d = 1.1$ μm are shown for three frequencies 6.78, 13.56 and 27.12 MHz. The particle is injected into the plasma from the middle of the discharge (central bulk plasma region) with two initial velocities $v_d = 0.25$ and $v_d = -0.25$ m s^{-1}. As we can see, the dust particle performs a damped oscillation around its equilibrium position close to the grounded sheath edge when the initial velocity is positive. In this case, the dust rises and can reach 9.2 mm from its initial position at 6.78 MHz, whereas at 13.56 MHz, the dust particle hits the grounded electrode. The same scenario is observed at 27.12 MHz with rapid hitting even if we give the same positive initial velocity to the dust particle. On the other hand, the dust particle at 6.78 MHz can also be suspended near the powered sheath edge despite the negative initial velocity, whereas the dust particle hits rapidly the powered electrode at 13.56 and 27.12 MHz, because the electric force becomes more important with the growth in the driving frequency and it is anti-parallel to the dust velocity. Note that if we examine the motion of a large dust particle with $r_d = 1.5$ μm in the same initial conditions taken in figure 9, the particle with positive initial velocity at 6.78 MHz rises but with a low height from the initial position compared with the small particle, whereas with negative initial velocity, the dust particle hits the powered electrode due to the increase in the gravitational force. On the other hand, if the driving frequency increases, this dust particle cannot rise in the sheath regions and rapidly hits the electrodes because the equilibrium position becomes closer to the electrodes, and the amplitude of oscillation initially becomes higher.

https://doi.org/10.1017/S0022377821000258 Published online by Cambridge University Press

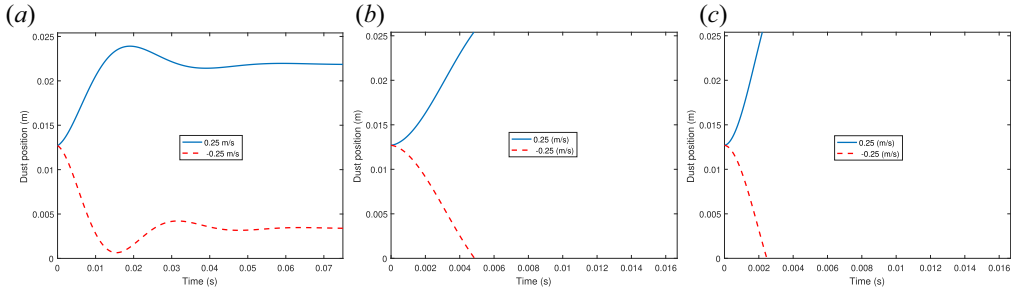

FIGURE 9. The trajectory of the dust particle with $r_d = 1.1$ μm released from the middle of the discharge for different initial velocities $v_d = 0.25$ m s^{-1} and $v_d = -0.25$ m s^{-1} at (*a*) 6.78 MHz, (*b*) 13.56 MHz and (*c*) 27.12 MHz, with $\rho_d = 2000$ kg m^{-3}.

6. Conclusion

In this paper, the effect of driving frequency on the dust particle dynamics in argon RF plasma discharge has been investigated by using a 1-D fluid model with the drift-diffusion approximation. In this model, we considered the continuity equations for electrons and ions, the momentum balance equation and the electron energy balance equation coupled to the Poisson equation. The dust particle charge has been calculated by the OML theory taking into account the contribution of the ion–neutral collision to the ion current. Then, the coefficients describing the amplification and damping of the dust particle oscillation have been determined and analysed. It has been shown that the driving frequency has a significant effect on the discharge characteristics such as electron density, electron temperature and the electric field, especially on the sheath thickness where an increase in the driving frequency leads to a decrease in the sheath width. Moreover, the equilibrium position of the dust particle becomes closer to the electrodes with a higher oscillation frequency for high driving frequencies. On the other hand, we demonstrated that the possibility of suspension of the dust particle can also be influenced by the initial conditions (position and velocity) depending on the driving frequency. Furthermore, at all driving frequencies, the trapping position for the small dust particle is relatively away from the powered electrode than for a particle with large radius owing to the decrease in the gravitational force. Finally, it was clearly shown that the driving frequency has a significant effect on the dust particle dynamics and suspension. Thus, it is possible to control the levitation height and the trajectory of the dust particle for different RF capacitive discharge conditions by varying the driving frequency.

Editor Edward Thomas, Jr. thanks the referees for their advice in evaluating this article.

Funding

This research received no specific grant from any funding agency, commercial or not-for-profit sectors.

Declaration of interests

The authors report no conflict of interest.

REFERENCES

AKDIM, M.R. & GOEDHEER, W.J. 2003 Modeling the effect of dust on the plasma parameters in a dusty argon discharge under microgravity. *J. Phys. Rev.* E **67** (6), 066407.

https://doi.org/10.1017/S0022377821000258 Published online by Cambridge University Press

BENYOUCEF, D., YOUSFI, M., BELMADANI, B. & SETTAOUTI, A. 2010 PIC MC using free path for the simulation of low-pressure RF discharge in argon. *J. IEEE Trans. Plasma Sci*. **38** (4), 902–908.

BLEECKER, K.D., BOGAERTS, A. & GOEDHEER, W.J. 2006 Modelling of nanoparticle coagulation and transport dynamics in dusty silane discharges. *J. New Phys*. **8** (9), 178–178.

BOEUF, J.P. 1987 Numerical model of RF glow discharges. *J. Phys. Rev.* A **36** (6), 2782–2792.

BOGAERTS, A., NEYTS, R. & GIJBELS, J.J. A.M. 2002 Gas discharge plasmas and their applications. *J. Spectrochim. Acta* B **57** (4), 609–658.

COLGAN, M.J., MEYYAPPAN, M. & MURNICK, D.E. 1994 Very high-frequency capacitively coupled argon discharges. *J. Plasma Sources Sci. Technol*. **3** (2), 181–189.

DAVOUDABADI, M. & MASHAYEK, F. 2006 Dust particle dynamics in low-pressure plasma reactor. *J. Appl. Phys*. **100** (8), 083302.

EL KAOUINI, M., CHATEI, H. & BOUGDIRA, J. 2014 Dynamics of dust particles in a collisional radio-frequency plasma sheath. *J. Phys. Scr*. **T161**, 014052.

EPSTEIN, P.S. 1924 On the resistance experienced by spheres in their motion through gases. *J. Phys. Rev*. **23** (6), 710–733.

GOEDHEER, W.J. & LAND, V. 2008 Simulation of dust voids in complex plasmas. *J. Plasma Phys. Control. Fusion* **50** (12), 124022.

GOEDHEER, W.J., LAND, V. & VENEMA, J. 2009 Modelling of voids in complex radio frequency plasmas. *J. Contrib. Plasma Phys*. **49** (4–5), 199–214.

GRAVES, D.B. 1994 Plasma processing. *J. IEEE Trans. Plasma Sci*. **22** (1), 31–42.

GRUBERT, G.K., BECKER, M.M. & LOFFHAGEN, D. 2009 Why the local-mean-energy approximation should be used in hydrodynamic plasma descriptions instead of the local-field approximation. *J. Phys. Rev.* E **80** (3), 036405.

HEINTZ, M.J. & HIEFTJE, G.M. 1995 Effect of driving frequency on the operation of a radiofrequency glow discharge emission source. *J. Spectrochim. Acta* B **50** (9), 1125–1141.

HORN, C., DAVOUDABADI, M. & SHOTORBAN, B. 2011 Effects of radiofrequency on dust particle dynamics in a plasma reactor. *J. Appl. Phys*. **110** (11), 113305.

HUANG, S. & GUDMUNDSSON, J.T. 2014 A current driven capacitively coupled chlorine discharge. *J. Plasma Sources Sci. Technol*. **23** (2), 025015.

HUTCHINSON, I.H. 2005 Spherical particle interaction with flowing plasma: computational discoveries. *AIP Conf. Proc*. **799** (1), 38–47.

HUTCHINSON, I.H. 2006 Collisionless ion drag force on a spherical grain. *J. Plasma Phys. Control. Fusion* **48** (2), 185–202.

IVLEV, A.V., KHRAPAK, S.A., ZHDANOV, S.K., MORFILL, G.E. & JOYCE, G. 2004 Force on a charged test particle in a collisional flowing plasma. *J. Phys. Rev. Lett*. **92** (20), 205007.

IVLEV, A.V., KONOPKA, U. & MORFILL, G. 2000 Influence of charge variation on particle oscillations in the plasma sheath. *J. Phys. Rev.* E **62** (2), 2739–2744.

IVLEV, A.V., ZHDANOV, S.K., KHRAPAK, S.A. & MORFILL, G.E. 2005 Kinetic approach for the ion drag force in a collisional plasma. *J. Phys. Rev.* E **71** (1), 016405.

KHRAPAK, S.A. 2013 Electron and ion thermal forces in complex (dusty) plasma. *J. Phys. Plasmas* **20** (1), 013703.

KHRAPAK, S.A., IVLEV, A.V., MORFILL, G.E. & THOMAS, H.M. 2002 Ion drag force in complex plasmas. *J. Phys. Rev.* E **66** (4), 046414.

KHRAPAK, S.A., RATYNSKAIA, S.V., ZOBNIN, A.V., USACHEV, A.D., YAROSHENKO, V.V., THOMA, M.H., KRETSCHMER, M., HÖFNER, H., MORFILL, G.E., PETROV, O.F., *et al.* 2005 Particle charge in the bulk of gas discharges. *J. Phys. Rev.* E **72** (1), 016406.

KITAJIMA, T., TAKEO, Y., NAKANO, N. & MAKABE, T. 1998 Effects of frequency on the two-dimensional structure of capacitively coupled plasma in Ar. *J. Appl. Phys*. **84** (11), 5928–5936.

LAND, V., MATTHEWS, L.S., HYDE, T.W. & BOLSER, D. 2010 Fluid modeling of void closure in microgravity noble gas complex plasmas. *J. Phys. Rev.* E **81** (5), 056402.

LIU, Y., BOOTH, J.P. & CHABERT, P. 2018 Effect of frequency on the uniformity of symmetrical RF CCP discharges. *J. Plasma Sources Sci. Technol*. **27** (5), 055012.

Liu, Y., Zhang, Q., Jiang, W., Lu, W.Q. & Wang, Y. 2012 Experimental validation and simulation of collisionless bounce-resonance heating in capacitively coupled radio-frequency discharges. *J. Plasma Sources Sci. Technol*. **21** (3), 035010.

Lymberopoulos, D.P. & Economou, D.J. 1993 Fluid simulations of glow discharges: effect of metastable atoms in argon. *J. Appl. Phys*. **73** (8), 3668–3679.

Matthews, L.S., Sanford, D.L., Kostadinova, E.G., Ashrafi, K.S., Guay, E. & Hyde, T.W. 2020 Dust charging in dynamic ion wakes. *J. Phys. Plasmas* **27** (2), 023703.

Mikikian, M., Cavarroc, M., Couëdel, L., Tessier, Y. & Boufendi, L. 2010 Dust particles in low-pressure plasmas: formation and induced phenomena. *J. Pure Appl. Chem*. **82** (6), 1273.

Nitter, T. 1996 Levitation of dust in rf and dc glow discharges. *J. Plasma Sources Sci. Technol*. **5** (1), 93–111.

Rakhimova, T.V., Braginsky, O.V., Ivanov, V.V., Kim, T.K., Kong, J.T., Kovalev, A.S., Lopaev, D.V., Mankelevich, Y.A., Proshina, O.V. & Vasilieva, O.N., *et al.* 2006 Experimental and theoretical study of RF plasma at low and high frequency. *J. IEEE Trans. Plasma Sci*. **34** (3), 867–877.

Samir, T., Liu, Y., Zhao, L. & Zhou, Y. 2017 Effect of driving frequency on electron heating in capacitively coupled RF argon glow discharges at low pressure. *J. Chin. Phys.* B **26** (11), 115201.

Schabel, M., Peterson, T., Sinclair, J. & Lynch, D. 1999 Characterization of trapped particles in rf plasmas. *J. Appl. Phys*. **86** (4), 1834–1842.

Sharma, S., Sen, A., Sirse, N., Turner, M.M. & Ellingboe, A.R. 2018 Plasma density and ion energy control via driving frequency and applied voltage in a collisionless capacitively coupled plasma discharge. *J. Phys. Plasmas* **25** (8), 080705.

Sharma, S., Sirse, N., Kaw, P.K., Turner, M.M. & Ellingboe, A.R. 2016 Effect of driving frequency on the electron energy distribution function and electron-sheath interaction in a low pressure capacitively coupled plasma. *J. Phys. Plasmas* **23** (11), 110701.

Surendra, M. & Graves, D.B. 1991 Capacitively coupled glow discharges at frequencies above 13.56 MHz. *J. Appl. Phys. Lett*. **59** (17), 2091–2093.

Tomme, E.B., Annaratone, B.M. & Allen, J.E. 2000 Damped dust oscillations as a plasma sheath diagnostic. *J. Plasma Sources Sci. Technol*. **9** (2), 87–96.

Vahedi, V., Birdsall, C.K., Lieberman, M.A., Dipeso, G. & Rognlien, T.D. 1993 Verification of frequency scaling laws for capacitive radio-frequency discharges using two-dimensional simulations. *J. Phys. Fluids* B **5** (7), 2719–2729.

Wilczek, S., Trieschmann, J., Schulze, J., Schuengel, E., Brinkmann, R.P., Derzsi, A., Korolov, I., Donkó, Z. & Mussenbrock, T. 2015 The effect of the driving frequency on the confinement of beam electrons and plasma density in low-pressure capacitive discharges. *J. Plasma Sources Sci. Technol*. **24** (2), 024002.

Zhao, H., Li, B., Wang, W., Hu, Y. & Wang, Y. 2016 Effect of excitation frequency on characteristics of mixture discharge in fast-axial-flow radio frequency-excited carbon dioxide laser. *J. Front. Optoelectron*. **9** (4), 592–598.

Zhao, L., Liu, Y. & Samir, T. 2018 Numerical study on discharge characteristics influenced by secondary electron emission in capacitive RF argon glow discharges by fluid modeling. *J. Chin. Phys.* B **27** (2), 025201.

Zhu, X., Chen, W., Zhang, S., Guo, Z., Hu, D. & Pu, Y. 2007 Electron density and ion energy dependence on driving frequency in capacitively coupled argon plasmas. *J. Phys.* D **40** (22), 7019–7023.